



Remarkable strengthening effects of cells in laser powder bed fusion-processed Inconel 718

Taichi Kikukawa, Takuya Ishimoto, Hyoung Seop Kim & Takayoshi Nakano

To cite this article: Taichi Kikukawa, Takuya Ishimoto, Hyoung Seop Kim & Takayoshi Nakano (24 Jun 2025): Remarkable strengthening effects of cells in laser powder bed fusion-processed Inconel 718, Materials Research Letters, DOI: [10.1080/21663831.2025.2522801](https://doi.org/10.1080/21663831.2025.2522801)

To link to this article: <https://doi.org/10.1080/21663831.2025.2522801>



© 2025 The Author(s). Published by Informa UK Limited, trading as Taylor & Francis Group.



[View supplementary material](#)



Published online: 24 Jun 2025.



[Submit your article to this journal](#)



[View related articles](#)



[View Crossmark data](#)

Remarkable strengthening effects of cells in laser powder bed fusion-processed Inconel 718

Taichi Kikukawa^a, Takuya Ishimoto^b, Hyoung Seop Kim^c and Takayoshi Nakano^b

^aDivision of Materials and Manufacturing Science, Graduate School of Engineering, The University of Osaka, Osaka, Japan; ^bAluminium Research Center, University of Toyama, Toyama, Japan; ^cDepartment of Materials Science and Engineering, Pohang University of Science and Technology, Pohang, South Korea; ^dAnisotropic Design & Additive Manufacturing Research Center, The University of Osaka, Osaka, Japan

ABSTRACT

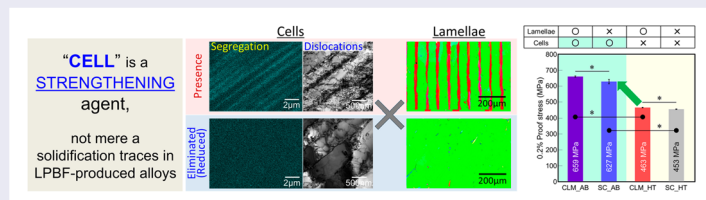
Alloys fabricated via laser powder bed fusion (LPBF) exhibit superior strength. This study investigates the individual strengthening effects of the nanometre-sized cellular and micrometre-sized crystallographic lamellar structures in the LPBF-fabricated Inconel 718 alloy by selectively eliminating these structures through heat treatment and a novel laser scanning strategy, respectively. While cellular structures increased the yield strength by approximately 38%, lamellar structures contributed to only a marginal 2% increase. This finding demonstrates the remarkable strengthening effect of cells on LPBF products. This study highlights that cells are not merely microstructures but are critical features governing the exceptional strength of LPBF products.

ARTICLE HISTORY

Received 5 March 2025

KEYWORDS

Laser powder bed fusion; cellular microstructures; lamellar structure; single crystal; strengthening



1. Introduction

Laser powder bed fusion (LPBF) enables precise fabrication of complex 3D structures. The small melt pools generated by the laser beam undergo rapid solidification, resulting in unique crystallographic textures and microstructures specific to LPBF. Notably, LPBF-produced materials exhibit significantly higher strength than their cast or wrought counterparts [1–3] primarily due to the formation of hierarchical microstructures [4–6]. However, because multiple microstructural features coexist in LPBF products depending on the alloy, the reinforcing effect of individual features remains unclear. Attempts to modify a single feature often fail because other features are typically affected.

The Inconel 718 (IN718) alloy is one of the most widely used materials in LPBF [7]. Two main microstructures have been reported in LPBF-fabricated IN718. First

is the crystallographic lamellar microstructure (CLM) [8], formed through a $\pm X$ scanning strategy ($\pm X_{SS}$) (Figure 1(a)) involving bidirectional laser scanning in the x -direction across each layer. The $\langle 011 \rangle // \text{BD}$ -oriented single-crystal (SC)-like texture commonly forms under the $\pm X_{SS}$ [9–12]. However, in Ni-based alloys, CLM formation is more common [8,13–16]. The $\langle 011 \rangle // \text{BD}$ -oriented SC-like texture develops owing to $\langle 001 \rangle$ -directed cell growth inclined $\pm 45^\circ$ from BD [12]. The CLM consists of grains with the same crystal growth behavior and $\langle 011 \rangle // \text{BD}$ orientation as the SC-like texture (main layer) and grains with $\langle 001 \rangle // \text{BD}$ orientation between main layers (sub-layer), stacked alternately in the y -direction (Figure 1(b and c)) [8]. In the sub-layer, $\langle 001 \rangle$ -directed cells grow parallel to BD in response to the vertical downward heat flow at the melt pool bottom [8]. Studies have

CONTACT Takayoshi Nakano ✉ nakano@mat.eng.osaka-u.ac.jp 📧 Division of Materials and Manufacturing Science, Graduate School of Engineering, The University of Osaka, 2-1, Yamadaoka, Suita, Osaka 565-0871, Japan; Takuya Ishimoto ✉ ishimoto@sus.u-toyama.ac.jp 📧 Aluminium Research Center, University of Toyama, 3190, Gofuku, Toyama 930-8555, Japan

Supplemental data for this article can be accessed online at <https://doi.org/10.1080/21663831.2025.2522801>.

© 2025 The Author(s). Published by Informa UK Limited, trading as Taylor & Francis Group.

This is an Open Access article distributed under the terms of the Creative Commons Attribution License (<http://creativecommons.org/licenses/by/4.0/>), which permits unrestricted use, distribution, and reproduction in any medium, provided the original work is properly cited. The terms on which this article has been published allow the posting of the Accepted Manuscript in a repository by the author(s) or with their consent.

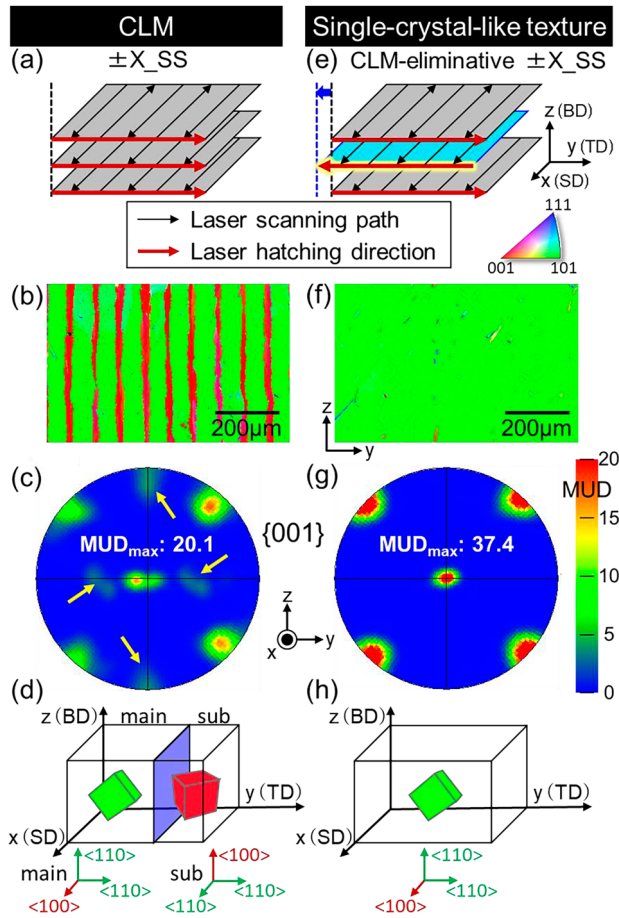


Figure 1. Schematics of the scanning strategy used to obtain (a) CLM and (e) SC-like texture. (b, f) Inverse pole figure (IPF) maps and (c, g) 001 pole figures representing the resulting texture, along with (d, h) illustrations of preferential crystallographic orientation in the product. The colour of the IPF map corresponds to the crystallographic orientation projected into the BD. The arrows in the pole figure (c) indicate the intensity derived from the crystal orientation of the sub-layer.

reported that CLMs enhance product strength at both room and high temperatures [8,17] and contribute to strength anisotropy [8].

Second is the nanometre-scale cellular microstructure characterized by micro-segregation, dislocation accumulation, and Laves phases at cell boundaries [18–20]. Segregation arises from compositional partitioning during solidification [21], and dislocations are likely introduced by thermal stresses during fabrication [18,22]. These cellular structures align with the $\langle 001 \rangle$ crystallographic direction, parallel to their growth, and significantly enhance LPBF-fabricated alloy strength [18]. However, their exact mechanical contributions remain uncertain owing to interactions with other microstructural features [19,23].

In this study, we quantitatively determined the mechanical contributions of these two microstructures

in LPBF-fabricated IN718 by using two microstructural modifications: (1) a new laser scanning strategy to eliminate the lamellar structure and (2) heat treatment conditions to selectively remove cellular microstructures without altering the crystallographic texture.

2. Materials and methods

A gas-atomized IN718 spherical powder (EOS, Germany) was used for LPBF fabrication with M290 printer (EOS). A $10 \times 10 \times 12 \text{ mm}^3$ rectangular product was fabricated under high-purity argon gas flow using $\pm X_{SS}$ (Figure 1(a)) with optimized laser conditions for CLM formation [8]. Next, a novel SS (CLM-eliminative $\pm X_{SS}$) was developed to eliminate the $\langle 001 \rangle // \text{BD}$ -oriented CLM sub-layer, while maintaining identical laser irradiation conditions. As epitaxial growth dominates the crystal orientation in upper layers, stable growth occurs when the antiparallel heat flow direction aligns with the $\langle 001 \rangle$ easy growth direction in cubic alloys. To disrupt this, we modified the scanning path by shifting it in the y -direction by half the hatch distance (Figure 1(e)). Additionally, the hatching direction was reversed between $-y$ and $+y$ for each layer to prevent the formation of diagonally propagating sub-grain boundaries (Supplementary Figure S1).

Some samples underwent heat treatment at 1080 °C—a temperature exceeding the solvus of γ' , γ'' , δ and Laves phases [18,24]—for 1 h in argon to eliminate the cellular microstructure, including Laves phases, without additional precipitation. For microstructural analysis the specimen cross-section was abraded using emery papers up to #4000 and then polished using colloidal silica for a mirror finish. The melt-pool trace and cellular microstructure were investigated using field-emission scanning electron microscopy (FE-SEM; JIB-4610F, JEOL, Japan). Crystallographic texture was analyzed using an electron backscatter diffraction (EBSD) system (NordlysMax³, Oxford Instruments, UK) on the FE-SEM, at a 20 kV accelerating voltage and 2 μm step interval. Inverse pole figure (IPF) maps and corresponding pole figures were calculated, with pole intensities expressed in multiple of uniform distribution (MUD). Transmission electron microscopy (TEM; JEM-3010, JEOL) at 300 kV was used to observe the cellular structure. TEM samples were thinned using a twin-jet machine (Tenupol-3, Struers, Denmark) with a solution comprising 20 vol% sulfuric acid and 80 vol% methanol at $-10 \text{ }^\circ\text{C}$.

For mechanical testing, $4 \times 4 \times 10 \text{ mm}^3$ rectangular specimens were cut from the product, and compression tests were performed ($N = 3$). Before testing, the side surfaces were polished to a mirror finish to observe

slip lines. The compression force was applied parallel to the 10 mm length (corresponding to BD) at an initial strain rate of $1.67 \times 10^{-4} \text{ s}^{-1}$. The individual and combined effects of the lamellar and cellular microstructures on the yield strength were statistically analyzed using two-way analysis of variance, with $P < 0.05$ considered statistically significant.

3. Results and discussion

Figure 1 compares the scanning strategies and the resulting crystallographic textures with and without CLM elimination. Under $\pm X_{SS}$, the expected CLM formed [8], while implementing the new scanning strategy yielded a highly oriented SC-like texture (Figure 1(f and g)), with homogeneous formation confirmed across entire specimen (Supplementary Figure S2). The preferential orientation of this texture aligned with that of the main layer in the CLM (Figure 1(d)), with $\langle 011 \rangle$ preferentially oriented in the BD (z -direction) and y -direction, and $\langle 001 \rangle$ in the scanning (x -) direction (Figure 1(h)). Notably, the MUD_{max} in the CLM (Figure 1(c)) was lower than that in the SC-like texture (Figure 1(g)). This is because the polar intensity distribution was dispersed owing to the presence of layers with two different orientations in the CLM specimen. The MUD_{max} calculated from the CLM main layer was 38.7, nearly equivalent to the orientation degree of SC-like texture. This indicates that the SC-like texture represents a CLM structure in which the $\langle 001 \rangle // BD$ -oriented sub-layer has been eliminated. Figure 2 illustrates how the sub-layer formation was suppressed. Under $\pm X_{SS}$, the $\langle 001 \rangle // BD$ -oriented sub-layer epitaxially grew upwards across multiple melt pools (thick white arrows in Figure 2(a)). In contrast, the sub-layer was rarely generated in the new scanning strategy (Figure 2(b)). When $\langle 001 \rangle // BD$ grains were accidentally generated near the center of the melt pool, they did not grow to the upper layers (Figure 2(c)) because these irregular grains with $\langle 001 \rangle // BD$ had an easy growth direction parallel to the BD, whereas the heat flow direction (red arrow in Figure 2(c)) in the melt pool of the next layer had a large angular difference from $\langle 001 \rangle$. Rather than inheriting the $\langle 001 \rangle // BD$ orientation, new grains were generated that grew $\langle 001 \rangle$ approximately along the heat flow direction. Incidentally, the $\langle 011 \rangle // BD$ -oriented region inherited its crystallographic orientation by epitaxial growth in a direct (white arrows) or side-branching fashion (light blue arrows) [25] from the immediate or adjacent solidification zone.

Tuning laser conditions and resultant melt pool dynamics is a key strategy for crystallographic texture control [8,26,27], but optimization can be limited by the

incompatibility between the conditions for texture stabilization and other targets such as sufficient densification [8]. In contrast, the scanning strategy of this study, which hindered the epitaxial growth of sub-layers by shifting the heat flow direction, effectively allowed to obtain SC-like texture with a prominent orientation (compare Figure 1(f) with the specimen produced at 360 W and 1400 mm s^{-1} in Figure 2 of reference [8]). Furthermore, texture reproducibility was remarkably high over across an entire region of specimens (Supplementary Figure S2) and even between specimens. Prominent SC-like textures are of great benefit in applications where grain boundaries can be a weak point, such as in turbine blades and components used in corrosive environments.

Similar SC-like textures could be obtained without reversing the hatch direction (Supplementary Figure S1). However, diagonally extending sub-grain boundaries were evident (Supplementary Figure S1(g)). Diagonal growth does not have the growth inhibition mechanism described in Figure 2(c) when stray grains occur; therefore, the stray grains can feasibly grow across layers (Supplementary Figure S1(f and g)). As a result, the overall texture intensity was reduced without reversing the hatch direction (Supplementary Figure S1(d and h)).

Next, the cellular microstructures were eliminated by heat treatment. In the as-built specimen, Nb, Mo, and Ti enrichment (Figure 3(a) and Supplementary Figure S3), dislocation accumulation (Figure 3(b)), and dispersed Laves phases (Figure 3(c)) in the intercell region were observed. After heat treatment, the segregation and Laves phases disappeared, and the dislocation density was largely decreased (Figure 3(e and f)). Dislocation density was reported to be reduced by half after heat treatment at $980 \text{ }^\circ\text{C}$ for 1 h [24]. In this study, the specimen was heat treated at $1080 \text{ }^\circ\text{C}$ for 1 h, and the dislocation density was expected to be even lower. As previously reported [18], spherical inclusions that do not disappear with heat treatment are carbides (arrows in Figures (c and f), typically NbC [18]) that exhibit a dissolution temperature of $1265 \text{ }^\circ\text{C}$ [28] and sizes of 20–150 nm [18]. The carbides did not show discernible size or distribution changes after heat treatment, and their strength contribution before and after heat treatment can be considered negligible. Importantly, changes in the crystallographic texture, including recrystallization and grain growth, were rarely observed, as shown in Figure 3(d and g) and Supplementary Figure S4, which were taken from the same region of the same specimen before and after heat treatment. The exhibited thermal stability of textures in IN718 produced in LPBF for short heat treatments at temperatures below $1100 \text{ }^\circ\text{C}$ was consistent with previous reports [29,30]. However, recrystallization has been reported after heat treatment at $1080 \text{ }^\circ\text{C}$ for more than

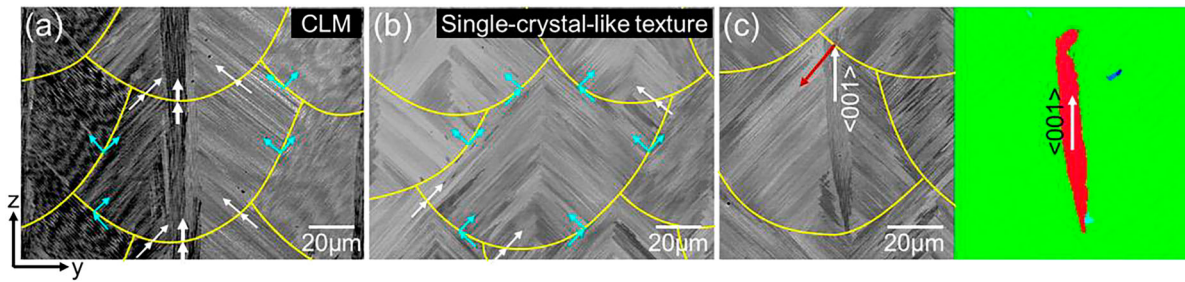


Figure 2. (a, b) SEM images of a cross-section perpendicular to the laser scanning direction, highlighting the cell microstructure and overlaid with a trace of the melt pool boundary. The difference in scanning strategies and the epitaxial growth at the melt pool boundaries are clearly depicted. White arrows indicate direct epitaxial growth at the melt pool boundary, while light blue arrows show epitaxial growth through 'side branching' [25], where the direction of cell growth is orthogonal, yet maintains the crystal orientation. (c) Grains with $\langle 001 \rangle //BD$ orientation suddenly appeared at the center of the melt pool. In the subsequent layer, the crystal orientation was not inherited because the $\langle 001 \rangle$ -oriented grain was in contact with the melt pool side wall.

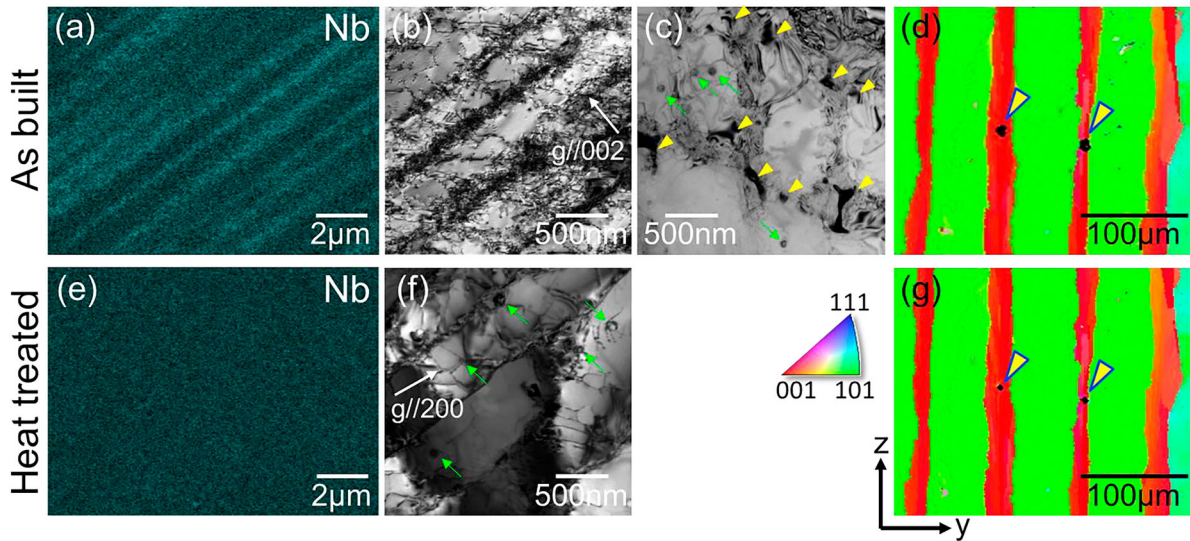


Figure 3. (a, e) EDS maps of Nb; (b, c, f) TEM bright-field images; (d, g) IPF maps ((a–d) before and (e–g) after heat treatment). The arrowheads and arrows in (c, f) indicate Laves phase and carbide particles, respectively, and the arrowheads in (d, g) indicate Vickers indentations made as location markers.

Table 1. Classification of the four samples prepared in this study based on the presence or absence of lamellae and cells.

	CLM_AB	SC_AB	CLM_HT	SC_HT
Lamellae	○	—	○	—
Cells	○	○	—	—

AB: as-built, HT: heat treated.

4 h or above 1100°C [18,30]. Therefore, the heat treatment condition adopted in this study can be considered to have reduced dislocations as much as possible.

Four types of specimens with distinct microstructure combinations were prepared by combining the aforementioned processes: CLM_AB with lamellae and cells, SC_AB with cells alone, CLM_HT with lamellae alone, and SC_HT without lamellae or cells (Table 1).

Figure 4 shows the variation in the yield stress. The cells significantly increased the yield stress by 38%

(453–627 MPa) for the specimen with the SC-like texture and by 42% (463–659 MPa) for the specimen with the CLM ($P < 0.05$) (Table 2). However, the increase in strength owing to the presence of lamellae, which was statistically significant ($P < 0.05$), was limited, ranging from 2.0% for specimens without cells to 5.1% for specimens with cells. To understand this slight but definite strength increase due to the lamellar structure, it is beneficial to consider the slip transfer at the interface between the $\langle 011 \rangle //BD$ -oriented main and $\langle 001 \rangle //BD$ -oriented sub-layers. Livingston and Chalmers [31] introduced the stress-transfer coefficient (N_{12}), which indicates the difficulty of slip propagation through the boundary between two crystals with different orientations. As the CLM obtained in this study exhibited prominent orientations of 38.7 and 50.3 in MUD_{max} for the main and sub-layers, respectively, and the main layer exhibited an orientation similar to that of

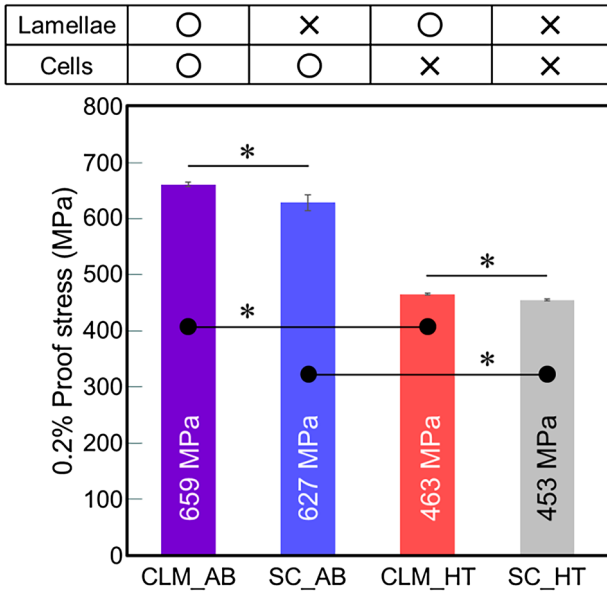


Figure 4. Comparison of yield stress as influenced by the presence of lamellae and cells. *: $P < 0.05$.

the SC-like texture, the slip transfer mechanism is relevant. When a plastic deformation occurs without accompanying cracking or a grain boundary slip, the continuity at the grain boundary of the adjacent grains must be maintained with identical shear stress values of crystal A (P_1) and B (P_2). Thus, the N_{12} was described as.

$$P_2 = P_1 \cdot N_{12} = P_1 \cdot [(e_1 \cdot e_2)(g_1 \cdot g_2) + (e_1 \cdot g_2)(e_2 \cdot g_1)], \quad (1)$$

where e_1 and e_2 are the slip plane normal directions and g_1 and g_2 are the slip directions (Supplementary Figure S5). A value of N_{12} closer to 1 indicates that the shear stress can easily be transferred to the slip system of the adjacent crystal. Therefore, the smaller N_{12} is, the more resistant the slip transmits through the interface, thereby increasing the strength. The N_{12} of a single-crystal is considered equal to 1. The N_{12} of the CLM was calculated as 0.819, indicating a moderate resistance to stress transfer between the $\langle 011 \rangle // \text{BD}$ and $\langle 001 \rangle // \text{BD}$ grains, which resulted in improved mechanical properties of the CLM specimens compared to those of the SC-like material. Furthermore, altering the loading axis changes the combination of active slip systems between the main and sub-layers, thereby decreasing the N_{12} value and increasing the contribution of the CLM to the strength [8].

With regard to strengthening by the cell microstructure, some researchers have argued that it exerts a similar contribution to that of grain boundaries (strengthening follows the Hall–Petch relationship) [32]. Other researchers have suggested that cells may not exhibit similar strengthening effect as grain boundaries but may offer

Table 2. Significance (P -values) of lamellae, cells, and their interaction on mechanical property. $P < 0.05$ considered statistically significant.

Factor	Effect of lamellae	Effect of cells	Interaction
P -value	0.0011	9.2×10^{-11}	0.030

resistance to grinding dislocations, but may not completely arrest them [19,33]. Some researchers argue that cells, which are essentially a type of elemental segregation, unlike grain boundaries, accumulate dislocations at high densities and strongly hinder their movement owing to the presence of chemically caused lattice disorder [34]. This study revealed that the cell is a dominant factor for the strength of LPBF-fabricated IN718, to the extent that it increased the yield stress by approximately 40%. The crystallographic $\langle 001 \rangle$ growth coincided with the direction of cell elongation; therefore, the $111 \langle 011 \rangle$ slip systems of IN718 with the FCC structure always interact with the high-density cell boundaries as it grids (Figure 5(a)). There is no path to avoid the cells, and it is subject to resistance by the cells independent of the loading axis. Figure 5(b and c) shows the slip traces that appeared on the sample surface. In the CLM_AB specimen with cells, the cell lines and dislocation traces intersected, clearly indicating that the dislocations grid through cell boundaries.

Interestingly, the two-way ANOVA showed a synergistic effect (interaction) between the strengthening effects of lamellae and cells (Table 2). Specifically, lamellae strengthening is enhanced when a lamellar structure is introduced into a cell-reinforced matrix. In general, strength increases owing to basic strengthening mechanisms, such as solid solution strengthening, precipitation strengthening, and grain boundary strengthening, and it can be linearly additive. The findings of this study suggest an interaction between the strengthening mechanisms of the unique LPBF microstructures, which is not simply an additive effect. Further, they provide insights into a more efficient strengthening effect than the additive effect of conventional strengthening. Furthermore, it has recently been shown that the introduction of additional artificial interfaces using compartments composed of these cells and lamella-containing materials as basic units and adjoining them horizontally and/or vertically in different orientations of the compartments further increases the strength of the material [35].

4. Conclusion

This study quantitatively determined the contributions of cellular and lamellar microstructures to the mechanical properties of LPBF-fabricated IN718 by selectively

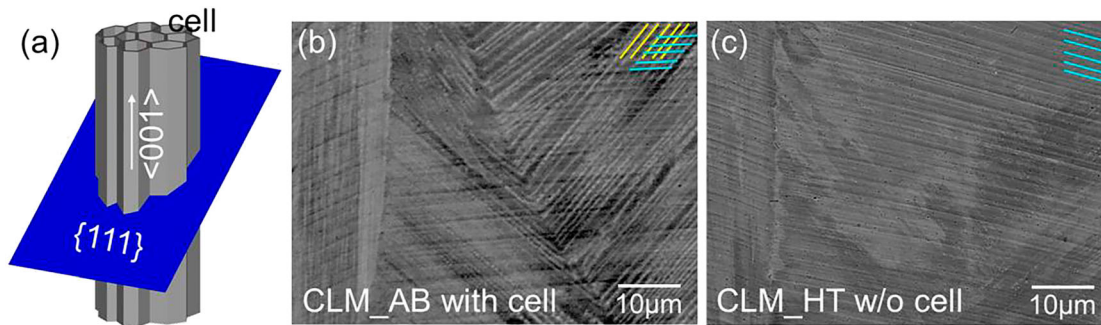


Figure 5. (a) Schematic representation of the cell network and its geometric relationship to the 111-slip plane in FCC crystals. Dislocations consistently interact with cells. Slip traces on the specimen surface after mechanical testing for (b) CLM_AB and (c) CLM_HT specimens. Yellow and light blue lines represent slip traces and cell boundaries, respectively.

eliminating them through distinct methods. A novel laser scanning strategy successfully removed the lamellar structure, while heat treatment erased the cellular microstructure without altering crystallographic texture. The results revealed that cellular structures were the dominant factor in the exceptional strength of LPBF-fabricated IN718, contributing significantly more than lamellar structures. These findings provide valuable insights into optimizing mechanical properties in alloys where cellular structures form naturally during solidification in LPBF. Rather than viewing them as mere microstructural features of LPBF-fabricated alloys introduced by rapid solidification and thermal cycling, cellular microstructures should be deliberately utilized as strengthening elements in alloy design for advanced mechanical performance.

Acknowledgments

This work was supported by CREST-Nanomechanics: Elucidation of macroscale mechanical properties based on understanding nanoscale dynamics for innovative mechanical materials (grant number JPMJCR2194) from the Japan Science and Technology Agency (JST).

Disclosure statement

No potential conflict of interest was reported by the author(s).

Funding

This work was supported by the Japan Science and Technology Agency (JST) [grant number JPMJCR2194].

Data availability statement

Data will be made available on request.

ORCID

Takuya Ishimoto  <http://orcid.org/0000-0003-0081-0591>

Hyoung Seop Kim  <http://orcid.org/0000-0002-3155-583X>

Takayoshi Nakano  <http://orcid.org/0000-0001-8052-1698>

References

- [1] Xuan Y, Chang J, Ou Y, et al. Heterogeneous structure architected by additive manufacturing: facile route towards strong and ductile steel. *Mater Res Lett.* 2024;12: 199–207. doi:10.1080/21663831.2024.2314145
- [2] Pazon C, Buttard M, Després A, et al. A novel laser powder bed fusion Al-Fe-Zr alloy for superior strength-conductivity trade-off. *Scr Mater.* 2022;219:114878. doi:10.1016/j.scriptamat.2022.114878
- [3] Gokcekaya O, Ishimoto T, Nishikawa Y, et al. Novel single crystalline-like non-equiatomc TiZrHfNbTaMo bio-high entropy alloy (BioHEA) developed by laser powder bed fusion. *Mater Res Lett.* 2023;12:274–280. doi:10.1080/21663831.2022.2147406
- [4] Wang YM, Voisin T, McKeown JT, et al. Additively manufactured hierarchical stainless steels with high strength and ductility. *Nat Mater.* 2018;17:63–71. doi:10.1038/nmat5021
- [5] Chen Z, Chen A, Jia Q, et al. Investigation of microstructures and strengthening mechanisms in an N-doped Co-Cr-Mo alloy fabricated by laser powder bed fusion. *Virtual Phys Prototyp.* 2023;18:e2219665. doi:10.1080/17452759.2023.2219665
- [6] Deng D, Peng RL, Brodin H, et al. Microstructure and mechanical properties of Inconel 718 produced by selective laser melting: sample orientation dependence and effects of post heat treatments. *Mater Sci Eng A.* 2018;713:294–306. doi:10.1016/j.msea.2017.12.043
- [7] Sanchez S, Smith P, Xu Z, et al. Powder bed fusion of nickel-based superalloys: a review. *Int J Mach Tool Manuf.* 2021;165:103729. doi:10.1016/j.ijmactools.2021.103729
- [8] Gokcekaya O, Ishimoto T, Hibino S, et al. Unique crystallographic texture formation in Inconel 718 by laser powder bed fusion and its effect on mechanical anisotropy. *Acta Mater.* 2021;212:116876. doi:10.1016/j.actamat.2021.116876
- [9] Ishimoto T, Morita N, Ozasa R, et al. Superimpositional design of crystallographic textures and macroscopic shapes via metal additive manufacturing—game-change in component design. *Acta Mater.* 2025;286:120709. doi:10.1016/j.actamat.2025.120709
- [10] Hagihara K, Nakano T. Control of anisotropic crystallographic texture in powder bed fusion additive manufacturing of metals and ceramics—a review. *JOM.* 2022;74:1760–1773. doi:10.1007/s11837-021-04966-7

- [11] He Y, Hou Y, Li X, et al. Texture, microstructure, and properties of Fe-Cr-Co permanent magnetic alloy fabricated by laser powder bed fusion in-situ alloying. *JOM*. 2024;76:4894–4907. doi:10.1007/s11837-024-06434-4
- [12] Ishimoto T, Hagihara K, Hisamoto K, et al. Crystallographic texture control of beta-type Ti-15Mo-5Zr-3Al alloy by selective laser melting for the development of novel implants with a biocompatible low Young's modulus. *Scr Mater*. 2017;132:34–38. doi:10.1016/j.scriptamat.2016.12.038
- [13] Wang P, Zhu Y, Lu N, et al. Controllable period of crystallographic lamellar microstructure in ZGH451 superalloy prepared by laser powder bed fusion. *J Mater Sci Technol*. 2025;211:239–243. doi:10.1016/j.jmst.2024.06.008
- [14] Pant P, Salvemini F, Proper S, et al. A study of the influence of novel scan strategies on residual stress and microstructure of L-shaped LPBF IN718 samples. *Mater Des*. 2022;214:110386. doi:10.1016/j.matdes.2022.110386
- [15] Xie X, Zhang F, Peng C, et al. Effect of scan strategy and substrate preheating on crack formation in IN738LC Ni-based superalloy during laser powder bed fusion. *Mater Charact*. 2025;221:114722. doi:10.1016/j.matchar.2025.114722
- [16] Hibino S, Todo T, Ishimoto T, et al. Control of crystallographic texture and mechanical properties of Hastelloy-X via laser powder bed fusion. *Crystals (Basel)*. 2021;11:1064. doi:10.3390/cryst11091064
- [17] Wang P, Liang J, Zhu Y, et al. Pursued strength-ductility synergy in Ni superalloys produced by laser powder bed fusion: crystallographic lamellar versus directionally solidified microstructure. *Mater Sci Eng A*. 2025;925:147838. doi:10.1016/j.msea.2025.147838
- [18] Tucho WM, Cuvillier P, Sjolyst-Kverneland A, et al. Microstructure and hardness studies of Inconel 718 manufactured by selective laser melting before and after solution heat treatment. *Mater Sci Eng A*. 2017;689:220–232. doi:10.1016/j.msea.2017.02.062
- [19] Li SH, Zhao Y, Radhakrishnan J, et al. A micropillar compression investigation into the plastic flow properties of additively manufactured alloys. *Acta Mater*. 2022;240:118290. doi:10.1016/j.actamat.2022.118290
- [20] Singh VK, Sahoo D, Amirthalingam M, et al. Dissolution of the laves phase and δ -precipitate formation mechanism in additively manufactured Inconel 718 during post printing heat treatments. *Addit Manuf*. 2024;81:104021. doi:10.1016/j.addma.2024.104021
- [21] Okugawa M, Saito K, Yoshima H, et al. Solute segregation in a rapidly solidified Hastelloy-X Ni-based superalloy during laser powder bed fusion investigated by phase-field and computational thermal-fluid dynamics simulations. *Addit Manuf*. 2024;84:104079. doi:10.1016/j.addma.2024.104079
- [22] Godec M, Zaefferer S, Podgornik B, et al. Quantitative multiscale correlative microstructure analysis of additive manufacturing of stainless steel 316L processed by selective laser melting. *Mater Charact*. 2020;160:110074. doi:10.1016/j.matchar.2019.110074
- [23] Zhu ZG, Nguyen QB, Ng FL, et al. Hierarchical microstructure and strengthening mechanisms of a CoCrFeNiMn high entropy alloy additively manufactured by selective laser melting. *Scr Mater*. 2018;154:20–24. doi:10.1016/j.scriptamat.2018.05.015
- [24] Gallmeyer TG, Moorthy S, Kappes BB, et al. Knowledge of process-structure-property relationships to engineer better heat treatments for laser powder bed fusion additive manufactured Inconel 718. *Addit Manuf*. 2020;31:100977. doi:10.1016/j.addma.2019.100977
- [25] Pham MS, Dovgvy B, Hooper PA, et al. The role of side-branching in microstructure development in laser powder-bed fusion. *Nat Commun*. 2020;11:749. doi:10.1038/s41467-020-14453-3
- [26] Jodi DE, Kitashima T, Koizumi Y, et al. Manufacturing single crystals of pure nickel via selective laser melting with a flat-top laser beam. *Addit Manuf Lett*. 2022;3:100066. doi:10.1016/j.addlet.2022.100066
- [27] Andreau O, Koutiri I, Peyre P, et al. Texture control of 316L parts by modulation of the melt pool morphology in selective laser melting. *J Mater Process Technol*. 2019;264:21–31. doi:10.1016/j.jmatprotec.2018.08.049
- [28] Chen M, Du Q, Shi R, et al. Phase field simulation of microstructure evolution and process optimization during homogenization of additively manufactured Inconel 718 alloy. *Front Mater*. 2022;9:1043249. doi:10.3389/fmats.2022.1043249
- [29] Popovich VA, Borisov EV, Popovich AA, et al. Impact of heat treatment on mechanical behaviour of Inconel 718 processed with tailored microstructure by selective laser melting. *Mater Des*. 2017;131:12–22. doi:10.1016/j.matdes.2017.05.065
- [30] Fayed EM, Saadati M, Shahriari D, et al. Effect of homogenization and solution treatments time on the elevated-temperature mechanical behavior of Inconel 718 fabricated by laser powder bed fusion. *Sci Rep*. 2021;11:2020. doi:10.1038/s41598-021-81618-5
- [31] Livingston JD, Chalmers B. Multiple slip in bicrystal deformation. *Acta Metall*. 1957;5:322–327. doi:10.1016/0001-6160(57)90044-5
- [32] Kim JG, Seol JB, Park JM, et al. Effects of cell network structure on the strength of additively manufactured stainless steels. *Met Mater Int*. 2021;27:2614–2622. doi:10.1007/s12540-021-00991-y
- [33] Liu L, Ding Q, Zhong Y, et al. Dislocation network in additively manufactured steel breaks strength–ductility trade-off. *Mater Today*. 2018;21:354–361. doi:10.1016/j.mattod.2017.11.004
- [34] Liu C, Wang Y, Zhang Y, et al. Deformation mechanisms of additively manufactured TiNbTaZrMo refractory high-entropy alloy: The role of cellular structure. *Int J Plast*. 2024;173:103884. doi:10.1016/j.ijplas.2024.103884
- [35] Mayama T, Ishimoto T, Tane M, et al. Novel strengthening mechanism of laser powder bed fusion manufactured Inconel 718: effects of customized hierarchical interfaces. *Addit Manuf*. 2024;93:104412. doi:10.1016/j.addma.2024.104412